DE GRUYTER Nanotechnology Reviews 2024; 13: 20240044

Research Article

Anil Ahlawat, Shilpa Chaudhary*, Karuppusamy Loganathan*, Mukesh Kumar Sharma, Mohamed Abbas, and Munugapati Bhavana

Heat convection and irreversibility of magneto-micropolar hybrid nanofluids within a porous hexagonal-shaped enclosure having heated obstacle

https://doi.org/10.1515/ntrev-2024-0044
received February 10, 2024; accepted May 24, 2024

Abstract: The significance of fluid flow under hydrothermal conditions within a hexagonal enclosure spans across numerous fields, underlining its broad applicability. However, our understanding of the free convection flow in these geometries is still limited despite its potential importance in science and technology. Therefore, this study numerically examines the heat convection and entropy generation within a porous hexagonal cavity containing a heated obstacle while subjected to a static magnetic field of intensity B_0. Micropolar hybrid nanofluid, composed of TiO_2 and graphene oxide nanoparticles, was used to fill the hexagonal cavity with water as the base fluid. The finite difference method is associated with successive over-relaxation, successive relaxation, and Gauss–Seidel techniques, which are used to solve the dimensionless governing partial differential equations. The desired outcomes are computed using in-house developed MATLAB codes. A specific result from prior research findings is used to validate the accuracy of these MATLAB codes. The outcomes demonstrate that an upsurge in Ra from 10^4 to 10^6 and ϕ_{hnf} from 0 to 4% leads to an enhancement in Nu_{ABW} to 53.05 and 3.14%, respectively. However, Nu_{ABW} diminishes by approximately 0.797 and 4.135% as Ha increases from 0 to 20 and K_0 increases from 2 to 7.5, respectively. The average Bejan number (Be_{avg}) consistently decreases as Ra increases, but Be_{avg} improves as Ha, vortex viscosity parameter (K_0), and ϕ_{hnf} increase. The most important finding of the work is that the position of the heated obstacle significantly influences both the heat convection and entropy generation processes.

Keywords: micropolar hybrid nanofluid, hexagonal cavity, heated obstacle, porous medium

Nomenclature

B_0	magnetic field intensity (T)
Be_{avg}	average Bejan number
Be_{local}	local BEJAN number
C_p	specific isobaric heat per unit mass (J kg^{-1} K^{-1})
Da	Darcy number
FDM	finite difference method
$\vec{g}$	gravitational acceleration (m s^{-2})
H	length and width of the square cavity (m)
Ha	Hartmann number
HNFs	hybrid nanofluids
J	micro-inertial density (m^{-2})
k	thermal conductivity (W m^{-1} K^{-1})
K_0	dimensionless vortex viscosity parameter
K	permeability of porous medium
MFs	micropolar fluids
N	dimensionless micro-rotation vector normal to the xy-plane
NFs	nanofluids

*** Corresponding author: Shilpa Chaudhary,** Department of Mathematics & Statistics, Manipal University Jaipur, Jaipur, Rajasthan, 303007, India, e-mail: chaudharyshilpa195@gmail.com
*** Corresponding author: Karuppusamy Loganathan,** Department of Mathematics & Statistics, Manipal University Jaipur, Jaipur, Rajasthan, 303007, India, e-mail: loganathankaruppusamy304@gmail.com
Anil Ahlawat: Department of Mathematics & Statistics, Manipal University Jaipur, Jaipur, Rajasthan, 303007, India, e-mail: anilahlawat409@gmail.com
Mukesh Kumar Sharma: Department of Mathematics, Guru Jambheshwar University of Science and Technology Hisar, Haryana-125001, India, e-mail: drms123@gmail.com
Mohamed Abbas: Electrical Engineering Department, College of Engineering, King Khalid University, Abha, 61421, Saudi Arabia, e-mail: mabas@kku.edu.sa
Munugapati Bhavana: Department of Computer Science and Engineering, MLR Institute of Technology, Hyderabad, Telangana, India, e-mail: bhavanamungapati@gmail.com

$\mathrm{Nu}_{\mathrm{ABW}}$	average Nusselt number
$\mathrm{Nu}_{\mathrm{LBW}}$	local Nusselt number
p	pressure (Pa)
P	dimensionless pressure
Pr	Prandtl number
Ra	Rayleigh number
S_{LEG}	dimensionless local entropy generation
S_{LFF}	local entropy generation due to fluid friction
S_{LHT}	local entropy generation due to heat transfer
S_{Total}	total entropy generation
T	dimensional temperature (K)
X, Y	dimensionless Cartesian co-ordinates
u, U	dimensional and dimensionless velocity along the x-axis (m s^{-1})
v, V	dimensional and dimensionless velocity along the y-axis (m s^{-1})
x, y	dimensional Cartesian co-ordinates (m)
ϵ	dorosity
κ	vortex viscosity parameter

Greek symbols

α	thermal diffusivity ($\mathrm{m}^2\ \mathrm{s}^{-1}$)
β	volumetric thermal expansion coefficient (K^{-1})
γ	spin gradient viscosity
μ	dynamic viscosity (kg $\mathrm{m}^{-1}\ \mathrm{s}^{-1}$)
ν	kinematic viscosity ($\mathrm{m}^{-2}\ \mathrm{s}^{-1}$)
ρ	density (kg m^{-3})
ϕ	volume fraction
ω	dimensionless vorticity function
ψ	dimensionless stream function
θ	dimensionless temperature
χ	material parameter

Subscripts

eff	effective
f	base fluid
GO	graphene oxide
hnf	hybrid nanofluid
TiO_2	titanium dioxide

1 Introduction

The modern world is primarily concerned with strengthening the heat transfer process as a result of the evolution of compact thermal gadgets. The boost in heat convection for numerous thermal devices can be achieved by the implementation of active and passive approaches. Active approaches involve mechanical aids, such as electric or magnetic fields, suction, injection, and radiative heat, to strengthen heat transfer. In contrast, passive processes involve modifying domains, making surface advancements, and employing fluid nanofluids (NFs). NFs are made up of liquids with low thermal conductivity (*e.g.*, ethylene glycol, kerosine oil, and water) and nanoparticles with a size range of less than 1–100 nm. Nanoparticles exhibit diverse characteristics in terms of shape, structure, and composition; this makes them appropriate for real-world applications, including extraction of oil, power plants, energy panels, electronic equipment, nuclear reactors, and fermentation production. In 1995, Choi and Eastman [1] explored the core concept of NFs to enhance the thermal properties of regular fluids. In recent years, NFs have gained prominence as a material to develop highly efficient thermal devices and have been substantially published, as indicated in the studies by Mansour *et al.* [2], Saha *et al.* [3], Saleem *et al.* [4], and Weng *et al.* [5]. Incorporating nanoparticles of metals (*e.g.*, iron, copper, silver, and gold) and metal oxides (*e.g.*, copper oxide, copper oxide, aluminum oxide, and titanium dioxide [TiO_2]) into conventional fluids forms NFs. Applications of NFs in the manufacturing sector are documented in the work of Wong and De Leon [6]. NFs possess an important role in the development of a new type of NF called hybrid nanofluids (HNFs), which involve the combination of two different types of nanoparticles. NFs contribute to the invention of a novel type of NF named HNF, which combines two distinct types of nanoparticles. The process of creating HNFs entails the dispersion of nanoparticles into a base fluid, which triggers several complexities, including achieving proper nanoparticle dispersion, ensuring stability, implementing surface modification, controlling viscosity, ensuring material compatibility, conducting characterization, and considering environmental impact. This particular family of NFs was initially investigated experimentally by Jana *et al.* [7]. Enhanced thermal conductivity can be attained by the advancement of HNFs, which surpass single nanoparticle-based NFs in terms of stability properties. Rashidi *et al.* [8] and Acharya [9,10] provide an extensive repository of studies on the assessment of viscosity and thermal efficiency, along with other physical attributes of HNFs. The need for quick heat transfer and cooling processes in thermal devices could be met by nanoparticles and hybrid nanoparticles using regular fluids.

The integration of magnetic fields into the study of fluid dynamics has attracted considerable interest because of its capacity to regulate and control fluid flows in diverse engineering contexts by introducing opposing Lorentz forces. However, there are a number of drawbacks to using a magnetic field in real-world scenarios, including high-energy consumption, complexity, cost, and limited heat transfer rates; compatibility issues with materials; environmental concerns; difficulties in scaling up; and safety and regulatory concerns. The advancement of flow features in a magneto-nanofluidic thermal system of recto-triangular shape during the transition from unsteady to steady dynamics is explored numerically by Manna *et al.* [11] and found that the flow profile is severely impacted by the inclined magnetic field. Therefore, investigating the mechanism of heat transfer and entropy production utilizing NF technology contained in a heated hexagonal cavity is a significant research field with the potential to enhance the effectiveness and efficacy of various engineering devices, as discussed by Rehman *et al.* [12], Khan *et al.* [13], Faraz *et al.* [14], and Nayak *et al.* [15].

Minimizing entropy production is an essential requirement to ensure efficient utilization of available energy. The second principle of thermodynamics suggests that the breakdown of a thermal device resulting from excessive heat must be controlled by enhancing the mechanism of heat convection in that device. Bejan [16,17] addressed the generation of entropy assessment to connect thermodynamics, heat transfer, and fluid mechanics in his work. Entropy generation in a two-dimensional laminar flow inside an inclined porous cavity, using Darcy's law, was carried out by Baytas [18]. Numerical assessments were carried out to analyze entropy production and convection of heat employing distinct thermal conditions in different cavities by Acharya [19], Ahlawat and Sharma [20,21], and Manna *et al.* [22]. Micropolar fluids (MFs) are a particular type of suspension that exhibit non-Newtonian fluid behavior. Eringen's [23,24] revolutionary contribution to the concept of MF established the property of skew-symmetry in the stress tensor, which arises from the micro-rotational movement of microconstituents. Papautsky *et al.* [25] first examined the comparison between computational and experimental findings for laminar flow using the MF theory. They found that the Darcy friction factor increases when working with MFs, which is contrary to the results obtained using the Navier–Stokes theory. Tayebi *et al.* [26] found that transmission of heat in an enclosure containing two hot cylinders filled with micropolar Al_2O_3–water NF improves as the Rayleigh number enhances and diminishes as the vortex viscosity (K) increases. An efficient convective heat transfer mechanism employing discrete heaters in an annulus packed with magnetohydrodynamic micropolar HNF was recently investigated by Ahlawat *et al.* [27].

The motivation behind this investigation stems from the pressing need to advance our understanding of heat transfer processes in complex fluidic systems and develop innovative strategies for enhancing thermal management efficiency. With the increasing demand for energy-efficient technologies and sustainable thermal solutions, there is a growing interest in exploring novel materials and techniques to improve heat transfer performance. This study presents a novel integration of multiple advanced concepts in fluid dynamics, nanotechnology, porous media, and magnetohydrodynamics. Significant focus has been given to the study of natural convection flow in porous hexagonal cavities. However, there has been limited research on the interaction of these flows with heated obstacles and the specific thermal boundary conditions that lead to entropy production. The aim of this investigation is to optimize heat transfer efficiency and maximize energy utilization in the equipment by improving NF technology and cavity design. In addition to its potential utility in micromixers, the hexagonal cavity was considered for its efficiency as a heat sink. An empirical investigation is carried out by progressively changing the different parameters to examine their effect on heat conveyance and entropy generation. The primary objective of this study is to investigate how heated obstacles and magnetic fields affect the transfer of heat, entropy production, and fluid flow capabilities in a porous hexagonal cavity saturated with micropolar HNFs utilizing the finite difference method (FDM) due to its capacity to offer a versatile, scalable, and precise numerical framework for solving differential equations in various scientific and engineering fields. This, in turn, aids in understanding and prediction of complex phenomena. The findings of this research make a valuable contribution to the field of thermal science and engineering and help in the advancement of highly effective heat-transfer devices that utilize HNFs.

2 Problem formulation

The current research centers on examining the impact of a heated obstacle and magnetic field on thermal convection and generation of entropy in a porous hexagonal cavity of equal side length H saturated with MF. TiO_2 and graphene oxide (GO) nanoparticles are employed owing to their excellent thermal properties, stability, adaptability, and compatibility with MFs. Figure 1 shows the physical model of the problem under consideration. The enclosure is subjected to a static magnetic field of strength $\vec{B}_0$ acting in the x-direction. The gravity vector, $\vec{g}$ acts in the opposite direction to the y-axis. The enclosure's bottom and top walls are subjected to thermal heating at a constant temperature denoted by T_h, while inclined walls are maintained at a

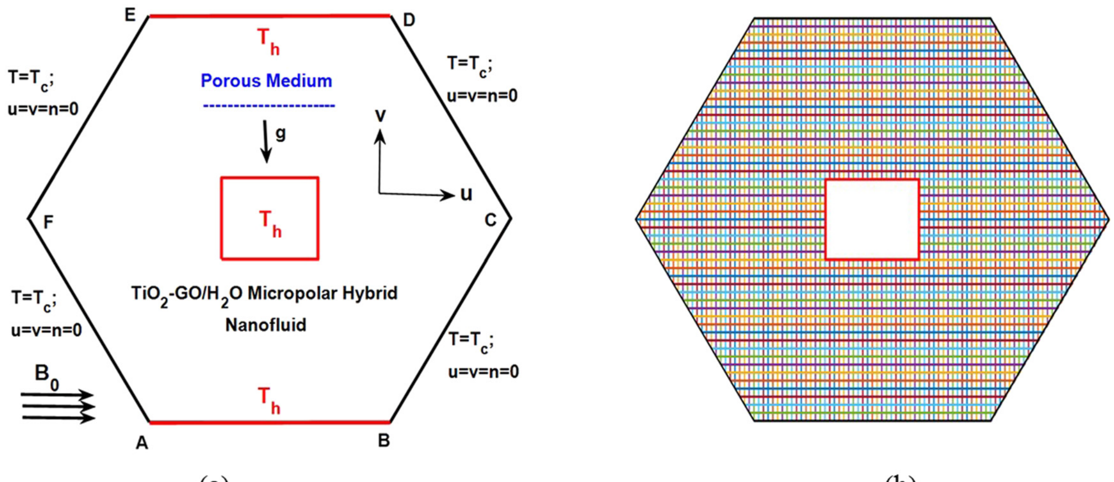

(a) (b)

Figure 1: Visualization of geometry under study (a) and grid generation (b).

temperature T_c, *i.e.*, $T_h > T_c$. The problem is modeled under the following assumptions:

1) 2D incompressible laminar steady flow.
2) The micropolar HNF, composed of TiO_2 and GO nanoparticles, is utilized to fill a hexagonal cavity with water as a regular fluid.
3) It is assumed that the joule heating and dissipative effects are insignificant.
4) Local thermal stability exists for all constituents, such as water and nanoparticles.

Table 1 lists the thermophysical properties of TiO_2, GO, and water. These are assumed to be temperature-independent despite the exception of the density utilized in the buoyancy term, which is estimated employing the Boussinesq approximation.

2.1 Basic governing equations

Following the principles of mass conservation, momentum conservation, angular momentum conservation, and energy conservation in the Cartesian coordinate system as described by Eringen [23,24] and Mansour *et al.* [30], the governing equations in their dimensional form for the steady-state conditions can be expressed as follows:

Continuity equation:

$$\frac{\mathrm{d}u}{\mathrm{d}x} + \frac{\mathrm{d}v}{\mathrm{d}y} = 0. \tag{1}$$

Linear momentum equations:

$$\rho_{\mathrm{hnf}}\left(u\frac{\mathrm{d}u}{\mathrm{d}x} + v\frac{\mathrm{d}u}{\mathrm{d}y}\right) = -\epsilon^2\frac{\mathrm{d}p}{\mathrm{d}x} + \epsilon(\mu_{\mathrm{hnf}} + \kappa)\left[\frac{\partial^2 u}{\partial x^2} + \frac{\partial^2 u}{\partial y^2}\right] + \epsilon^2\kappa\frac{\partial n}{\partial y} - \epsilon^2\frac{\mu_{\mathrm{hnf}}}{K}u, \tag{2}$$

$$\begin{aligned}\rho_{\mathrm{hnf}}\left(u\frac{\mathrm{d}v}{\mathrm{d}x} + v\frac{\mathrm{d}v}{\mathrm{d}y}\right) &= -\epsilon^2\frac{\mathrm{d}p}{\mathrm{d}y} + \epsilon(\mu_{\mathrm{hnf}} + \kappa)\left[\frac{\partial^2 v}{\partial x^2} + \frac{\partial^2 v}{\partial y^2}\right] \\ &\quad - \epsilon^2\kappa\frac{\partial n}{\partial x} + \epsilon^2(\rho\beta)_{\mathrm{hnf}}(T - T_c)\vec{g} - \sigma_{\mathrm{hnf}}B_0^2 v \\ &\quad - \epsilon^2\frac{\mu_{\mathrm{hnf}}}{K}v.\end{aligned} \tag{3}$$

Angular momentum equation:

Table 1: Thermophysical characteristics of H_2O, TiO_2, and GO as given in the studies of Pal and Mandal [28] and Al-Sankoor *et al.* [29]

Physical parameter	**C_p (J kg^{-1} K^{-1})**	**ρ (kg m^{-3})**	**k (W m^{-1} K^{-1})**	**β (K^{-1})**	**σ (Ω^{-1} m^{-1})**
H_2O	4,179	997.1	0.613	21×10^{-5}	5.5×10^{-6}
TiO_2	686.2	4,250	8.9538	0.9×10^{-5}	2.6×10^{6}
GO	717	1,800	5,000	2.84×10^{-4}	1.1×10^{-5}

$$\rho_{\mathrm{hnf}}\left(u\frac{\mathrm{d}n}{\mathrm{d}x}+v\frac{\mathrm{d}n}{\mathrm{d}y}\right)=\epsilon\frac{\gamma_{\mathrm{hnf}}}{j}\left[\frac{\partial^2 n}{\partial x^2}+\frac{\partial^2 n}{\partial y^2}\right]-\epsilon\frac{2\kappa}{j}n+\frac{\kappa}{j}\left[\frac{\partial v}{\partial x}-\frac{\partial u}{\partial y}\right]. \tag{4}$$

Energy equation:

$$\left(u\frac{\mathrm{d}T}{\mathrm{d}x}+v\frac{\mathrm{d}T}{\mathrm{d}y}\right)=\alpha_{\mathrm{eff}}\left[\frac{\partial^2 T}{\partial x^2}+\frac{\partial^2 T}{\partial y^2}\right], \tag{5}$$

$$\alpha_{\mathrm{hnf}}=\frac{k_{\mathrm{hnf}}}{(\rho C_{\mathrm{p}})_{\mathrm{hnf}}};\alpha_{\mathrm{eff}}=\frac{k_{\mathrm{eff}}}{(\rho C_{\mathrm{p}})_{\mathrm{hnf}}},$$

where $k_{\mathrm{eff}}=(1-\varepsilon)k_{\mathrm{s}}+\varepsilon k_{\mathrm{hnf}}$.

The thermal conductivity of the porous medium is $k_{\mathrm{s}}=0.845$ W/mK and its porosity is set at $\varepsilon=0.398$ making it identical to 3 mm glass beads. The spin-gradient viscosity (γ_{hnf}) can be determined using the studies of Ahmadi [31], Rees and Pop [32], and Ishak *et al.* [33] as follows:

$$\gamma_{\mathrm{hnf}}=\left(\mu_{\mathrm{hnf}}+\frac{\kappa}{2}\right)j. \tag{6}$$

The velocity components in the x and y directions are u and v, respectively, and T is the fluid's temperature. The boundary conditions in dimensional form that apply to the problem under consideration are as follows:

$$\left.\begin{array}{l}\text{top and bottom walls}: u=0,\ v=0, n=0,\ T=T_{\mathrm{h}}\\ \text{left and right inclined walls}: u=0,\ v=0, n=0,\\ T=T_{\mathrm{c}}\\ \text{at the heated obstacle}: u=0,\ v=0, n=0,\ T=T_{\mathrm{h}}\end{array}\right\}. \tag{7}$$

The subsequent metrics provided in equation (8) were employed to transform the basic equations into a dimensionless form [21]:

$$\begin{gathered}X=\frac{x}{H};Y=\frac{y}{H};\theta=\frac{T-T_{\mathrm{c}}}{T_{\mathrm{h}}-T_{\mathrm{c}}};K_0=\frac{\kappa}{\mu_{\mathrm{f}}};\mathrm{Pr}=\frac{\nu_{\mathrm{f}}}{\alpha_{\mathrm{f}}};\\ \mathrm{Ha}=B_0H\sqrt{\frac{\sigma_{\mathrm{f}}}{\mu_{\mathrm{f}}}};N=\frac{nH^2}{\alpha_{\mathrm{f}}};U=\frac{uH}{\alpha_{\mathrm{f}}};V=\frac{vH}{\alpha_{\mathrm{f}}};\\ \Delta T=T_{\mathrm{h}}-T_{\mathrm{c}},\ \mathrm{Ra}=\frac{\vec{g}\beta_{\mathrm{f}}(T_{\mathrm{h}}-T_{\mathrm{c}})H^3}{\nu_{\mathrm{f}}\alpha_{\mathrm{f}}}.\end{gathered} \tag{8}$$

The thermophysical characteristics, which are affected by the volume concentration of both $\mathrm{TiO_2}$ ($\phi_{\mathrm{TiO_2}}$) and GO (ϕ_{GO}) nanoparticles, are taken according to Ghalambaz *et al.* [34] and described by the subsequent associations provided in equation (9):

$$\begin{aligned}&\phi_{\mathrm{hnf}}=\phi_{\mathrm{GO}}+\phi_{\mathrm{TiO_2}},\\ &\rho_{\mathrm{hnf}}=(1-\phi_{\mathrm{hnf}})\rho_{\mathrm{f}}+\phi_{\mathrm{GO}}\rho_{\mathrm{GO}}+\phi_{\mathrm{TiO_2}}\rho_{\mathrm{TiO_2}},\\ &(\rho\beta)_{\mathrm{hnf}}=(1-\phi_{\mathrm{hnf}})\rho_{\mathrm{f}}+\phi_{\mathrm{GO}}(\rho\beta)_{\mathrm{GO}}+\phi_{\mathrm{TiO_2}}(\rho\beta)_{\mathrm{TiO_2}},\\ &(\rho \mathrm{C_p})_{\mathrm{hnf}}=(1-\phi_{\mathrm{hnf}})\rho_{\mathrm{f}}+\phi_{\mathrm{GO}}(\rho C_{\mathrm{p}})_{\mathrm{GO}}+\phi_{\mathrm{TiO_2}}(\rho C_{\mathrm{p}})_{\mathrm{TiO_2}},\\ &\alpha_{\mathrm{hnf}}=\frac{k_{\mathrm{hnf}}}{(\rho C_{\mathrm{p}})_{\mathrm{hnf}}}.\end{aligned} \tag{9}$$

k_{hnf} and μ_{hnf} are determined according to Maxwell [35] and Brinkman [36] as given in equations (10) and (11):

$$k_{\mathrm{hnf}}=\left[\frac{\left(\frac{\phi_{\mathrm{GO}}k_{\mathrm{GO}}+\phi_{\mathrm{TiO_2}}k_{\mathrm{TiO_2}}}{\phi_{\mathrm{hnf}}}+2k_{\mathrm{f}}\right)+2(\phi_{\mathrm{GO}}k_{\mathrm{GO}}+\phi_{\mathrm{TiO_2}}k_{\mathrm{TiO_2}})-2\phi_{\mathrm{hnf}}k_{\mathrm{f}}}{\left(\frac{\phi_{\mathrm{GO}}k_{\mathrm{GO}}+\phi_{\mathrm{TiO_2}}k_{\mathrm{TiO_2}}}{\phi_{\mathrm{hnf}}}+2k_{\mathrm{f}}\right)-(\phi_{\mathrm{GO}}k_{\mathrm{GO}}+\phi_{\mathrm{TiO_2}}k_{\mathrm{TiO_2}})+\phi_{\mathrm{hnf}}k_{\mathrm{f}}}\right]k_{\mathrm{f}}, \tag{10}$$

$$\mu_{\mathrm{hnf}}=\frac{\mu_{\mathrm{f}}}{(1-\phi_{\mathrm{hnf}})^{2.5}}, \tag{11}$$

$$\frac{\sigma_{\mathrm{hnf}}}{\sigma_{\mathrm{f}}}=1+\frac{3\phi_{\mathrm{hnf}}(((\sigma_{\mathrm{GO}}\phi_{\mathrm{GO}}+\sigma_{\mathrm{TiO_2}}\phi_{\mathrm{TiO_2}})/\phi_{\mathrm{hnf}})-\sigma_{\mathrm{f}})}{((\sigma_{\mathrm{GO}}\phi_{\mathrm{GO}}+\sigma_{\mathrm{TiO_2}}\phi_{\mathrm{TiO_2}})/\phi_{\mathrm{hnf}})+2\sigma_{\mathrm{f}}-\phi_{\mathrm{hnf}}(((\sigma_{\mathrm{GO}}\phi_{\mathrm{GO}}+\sigma_{\mathrm{TiO_2}}\phi_{\mathrm{TiO_2}})/\phi_{\mathrm{hnf}})-\sigma_{\mathrm{f}})}. \tag{12}$$

The stream function technique is employed to eliminate the pressure gradients from the momentum equations, *i.e.*, $U=\frac{\partial\psi}{\partial Y}$ and $V=-\frac{\partial\psi}{\partial X}$ and vorticity $\omega=\frac{\partial V}{\partial X}-\frac{\partial U}{\partial Y}$. The dimensionless metrics specified in equation (8) are used to derive the dimensionless equations as follows:

$$\frac{\partial^2\psi}{\partial X^2}+\frac{\partial^2\psi}{\partial Y^2}=-\omega. \tag{13}$$

Vorticity equation:

$$\begin{aligned}&\left[\frac{\partial\psi}{\partial Y}\frac{\partial\omega}{\partial X}-\frac{\partial\psi}{\partial X}\frac{\partial\omega}{\partial Y}\right]\\ &=\left(\frac{\rho_{\mathrm{f}}}{\rho_{\mathrm{hnf}}}\right)\epsilon\mathrm{Pr}\left(\frac{\mu_{\mathrm{hnf}}}{\mu_{\mathrm{f}}}+K_0\right)\left[\frac{\partial^2\omega}{\partial X^2}+\frac{\partial^2\omega}{\partial Y^2}\right]\\ &\quad-\left(\frac{\rho_{\mathrm{f}}}{\rho_{\mathrm{hnf}}}\right)\epsilon^2(K_0\mathrm{Pr})\left[\frac{\partial^2 N}{\partial X^2}+\frac{\partial^2 N}{\partial Y^2}\right]\\ &\quad-\left(\frac{\rho_{\mathrm{f}}}{\rho_{\mathrm{hnf}}}\right)\epsilon^2\left(\frac{\mathrm{Pr}}{\mathrm{Da}}\right)\left(\frac{\mu_{\mathrm{hnf}}}{\mu_{\mathrm{f}}}\right)\omega\\ &\quad+\left(\frac{\beta_{\mathrm{hnf}}}{\beta_{\mathrm{f}}}\right)\epsilon^2\mathrm{Ra}\,\mathrm{Pr}\frac{\partial\theta}{\partial X}+\left(\frac{\sigma_{\mathrm{hnf}}}{\sigma_{\mathrm{f}}}\right)\left(\frac{\rho_{\mathrm{f}}}{\rho_{\mathrm{hnf}}}\right)\mathrm{Ha}^2\mathrm{Pr}\epsilon^2\left[\frac{\partial^2\psi}{\partial X^2}\right].\end{aligned} \tag{14}$$

Angular momentum equation:

$$\left[\frac{\partial\psi}{\partial Y}\frac{\partial N}{\partial X} - \frac{\partial\psi}{\partial X}\frac{\partial N}{\partial Y}\right] = \left(\frac{\rho_{\mathrm{f}}}{\rho_{\mathrm{hnf}}}\right)\left(\frac{\mu_{\mathrm{hnf}}}{\mu_{\mathrm{f}}} + \frac{K_0}{2}\right)\epsilon\mathrm{Pr}\left[\frac{\partial^2 N}{\partial X^2} + \frac{\partial^2 N}{\partial Y^2}\right] - 2\chi\epsilon K_0\mathrm{Pr}\left(\frac{\rho_{\mathrm{f}}}{\rho_{\mathrm{hnf}}}\right)N + \chi K_0\mathrm{Pr}\left(\frac{\rho_{\mathrm{f}}}{\rho_{\mathrm{hnf}}}\right)\omega. \tag{15}$$

Energy equation:

$$\left[\frac{\partial\psi}{\partial Y}\frac{\partial\theta}{\partial X} - \frac{\partial\psi}{\partial X}\frac{\partial\theta}{\partial Y}\right] = \left(\frac{\alpha_{\mathrm{eff}}}{\alpha_{\mathrm{f}}}\right)\left[\frac{\partial^2\theta}{\partial X^2} + \frac{\partial^2\theta}{\partial Y^2}\right]. \tag{16}$$

For this particular given physical model, the non-dimensional boundary conditions are as follows:

$$\left.\begin{array}{ll}
\text{top and bottom walls} & : U = V = 0; N = 0, \\
 & \theta = 1 \quad \text{and} \quad \omega = -\left(\frac{\partial^2\psi}{\partial X^2}\right) \\
\text{left and right inclined walls} & : U = V = 0; N = 0; \\
 & \theta = 0 \quad \text{and} \quad \omega = -\left(\frac{\partial^2\psi}{\partial Y^2}\right) \\
\text{at the heated obstacle} & : U = V = 0; N = 0; \\
 & \theta = 1 \quad \text{and} \quad \omega = -\left(\frac{\partial^2\psi}{\partial X^2}\right) \\
 & \quad \text{and} \quad \omega = -\left(\frac{\partial^2\psi}{\partial Y^2}\right)
\end{array}\right\}. \tag{17}$$

On the bottom heated wall of the hexagonal cavity, the local Nusselt number ($\mathrm{Nu}_{\mathrm{LBW}}$) and average Nusselt number ($\mathrm{Nu}_{\mathrm{ABW}}$) can be expressed as

$$\mathrm{Nu}_{\mathrm{LBW}} = -\left(\frac{k_{\mathrm{eff}}}{k_{\mathrm{f}}}\right)\left(\frac{\partial\theta}{\partial Y}\right) \quad \text{and} \quad \mathrm{Nu}_{\mathrm{ABW}} = \frac{1}{H}\int_0^H \mathrm{Nu}_{\mathrm{LBW}}\,\mathrm{d}Y, \tag{18}$$

where H is the length of the heated wall of the hexagonal cavity.

2.2 Entropy generation analysis

In light of Seyyedi *et al.* [37], dimensionless local entropy generation (S_{LEG}) in its dimensionless form considering the magnetic field can be defined as

$$S_{\mathrm{LEG}} = \frac{k_{\mathrm{eff}}}{k_{\mathrm{f}}}\left[\left(\frac{\partial\theta}{\partial X}\right)^2 + \left(\frac{\partial\theta}{\partial Y}\right)^2\right] + \left(\frac{\chi}{\mathrm{Da}}\right)\left(\frac{\mu_{\mathrm{hnf}}}{\mu_{\mathrm{f}}} + K_0\right)(U^2 + V^2) + \chi\left(\frac{\mu_{\mathrm{hnf}}}{\mu_{\mathrm{f}}} + K_0\right)\left[2\left(\frac{\partial U}{\partial X}\right)^2 + 2\left(\frac{\partial V}{\partial Y}\right)^2 + \left(\frac{\partial U}{\partial Y} + \frac{\partial V}{\partial X}\right)^2\right] + \left(\frac{\sigma_{\mathrm{hnf}}}{\sigma_{\mathrm{f}}}\right)\chi\mathrm{Ha}^2V^2, \tag{19}$$

where $\xi = \frac{\mu_{\mathrm{f}}T_0}{k_{\mathrm{f}}}\left(\frac{\alpha_{\mathrm{f}}^2}{H(\Delta T)^2}\right)$ denotes the irreversible distribution.

The estimated value of the total entropy generation (S_{Total}) can be obtained by

$$S_{\mathrm{Total}} = \int_V S_{\mathrm{LEG}}\,\mathrm{d}V. \tag{20}$$

The local ($\mathrm{Be}_{\mathrm{local}}$) and average ($\mathrm{Be}_{\mathrm{avg}}$) Bejan number can be defined as

$$\mathrm{Be}_{\mathrm{local}} = \frac{S_{\mathrm{LEGHT}}}{S_{\mathrm{LEG}}} \quad \text{and} \quad \mathrm{Be}_{\mathrm{avg}} = \int_V \mathrm{Be}_{\mathrm{local}}\,\mathrm{d}V, \tag{21}$$

where $S_{\mathrm{LEGHT}} = \frac{k_{\mathrm{eff}}}{k_{\mathrm{f}}}\left[\left(\frac{\partial\theta}{\partial X}\right)^2 + \left(\frac{\partial\theta}{\partial Y}\right)^2\right]$ refers to the irreversibility resulting from the transfer of heat.

3 Numerical solution and code validation

To solve non-dimensional governing equations (13)–(16) numerically, together with dimensionless boundary conditions given above in equation (17), the FDM is employed. The in-house developed MATLAB codes are used to compute the desired results. To achieve solution reliability, the upwind scheme was used to handle the convective terms of the momentum and energy equations. When the condition $\frac{\sum_{i,j}|\varphi_{i,j}^{k+1} - \varphi_{i,j}^{k}|}{\sum_{i,j}|\varphi_{i,j}^{k+1}|} \le 10^{-7}$ is met, the iteration is over, where φ represents any of the computed value from ψ, ω, N, and θ. For the permissible error of order 10^{-7}, the number of maximum iterations included are 10^4. For this computation, the CPU time is approximately 17 min. The specific results of Ghalambaz *et al.* [34], Ali *et al.* [38, and Ilis *et al.* [39] are used to validate the accuracy of these MATLAB codes, and the results are compared in Figure 2 and Table 2. The excellent correlation between the outcomes confirms the validity of our simulation. The grid independence of the self-developed MATLAB codes was examined by computing the average Nusselt number ($\mathrm{Nu}_{\mathrm{ABW}}$) and average Bejan number ($\mathrm{Be}_{\mathrm{avg}}$) at the bottom heated wall, as displayed in Table 3. Hence, the 241 × 121 grids were employed to achieve the desired outcomes.

4 Results and discussion

This section depicts the empirical findings through graphical representation to demonstrate the influences of the examined parameters on the heat convection, entropy generation, and flow characteristics within a porous,

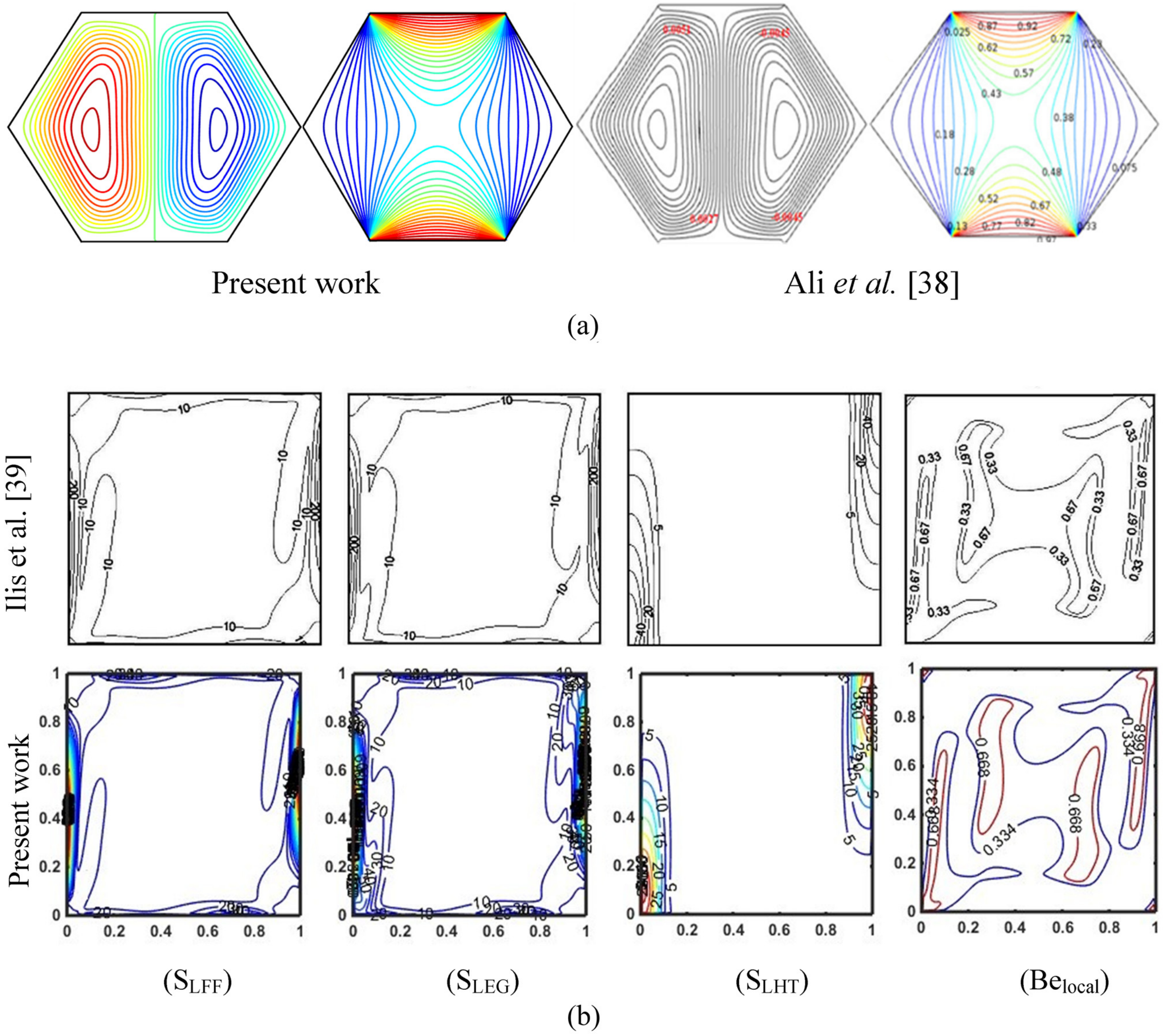

Figure 2: Validation of the present codes against (a) Ali *et al.* [38] and (b) Ilis *et al.* [39].

regular hexagonal cavity having a heated obstacle at its center. The micropolar HNF, composed of TiO_2 and GO nanoparticles, was utilized to fill a hexagonal cavity with water as a regular fluid. The numerical outcomes were examined by examining isotherm lines, streamlines, isolines of micro-rotation, local Bejan number, local entropy

Table 2: Average Nusselt number compared with the results of Ghalambaz *et al.* [34] while validating the source code at Ra = 10^4, Pr = 6.2, and R_k = 10

	ϕ_{hnf} = 0%		ϕ_{hnf} = 1%	
Grid size	**Ghalambaz *et al.* [34]**	**Current study**	**Ghalambaz *et al.* [34]**	**Current study**
50 × 50	2.1536	2.1536	2.1490	2.1840
70 × 70	2.1530	2.1436	2.1485	2.1462
100 × 100	2.1527	2.1455	2.1483	2.1509
120 × 120	2.1527	2.1581	2.1482	2.1578
140 × 140	2.1526	2.1509	2.1482	2.1662

Table 3: Grid independency test when Pr = 6.26, Ra = 10^5, Da = 10^{-3}, Ha = 10, K_0 = 2, and ϕ_{hnf} = 4%

Grid size	161 × 81	181 × 91	201 × 101	221 × 111	241 × 121
Nu_{ABW}	10.6531	10.6846	10.6986	10.6995	10.7000
Be_{avg}	0.43610	0.45973	0.48489	0.48545	0.48580

generation, and average Nusselt number for various values of parameters within the range $0 \le \text{Ha} \le 20$, $10^{-2} \le \text{Da} \le 10^{-4}$, $10^4 \le \text{Ra} \le 10^6$, $0\% \le \phi_{\text{hnf}} \le 4\%$, and $2 \le K_0 \le 7.5$, while the Prandtl number (Pr) remains constant at a value of 6.26. The impacts of the physical variables employed in this study were thoroughly explored. Figure 3 demonstrates the significance of Ra on the behaviors of streamlines, isotherms, isolines of micro-rotation, dimensionless local entropy generation (S_{LEG}), and local Bejan number (Be_{local}) considering Ha = 10, Da = 10^{-3}, K_0 = 2, and ϕ_{hnf} = 4%. Figure 3 shows two directional circulations adjacent to the obstacle inside the enclosure for different Ra values. The fluid adjacent to the thermally heated horizontal sides of the cavity is significantly hotter than the fluid adjacent to the cold slanted walls. Therefore, the density of fluid near the hot walls is lesser than that of fluids close to cold walls.

This causes fluid to flow in two directions: upward and downward through the slanted cold walls close to the center of the bottom wall, where it continues to move from bottom to top. As a result, the streamlines move up and down in parallel orientations adjacent to the block depicted in Figure 3.

Furthermore, the graphical representations of the streamlines demonstrate that the strength and intensity of flow rotation increase as Ra increases from 10^4 to 10^6 because as Ra increases, the buoyancy forces become stronger, causing fluid to move at a higher velocity. It is worth mentioning that the isotherms exhibit higher concentration near the edges of the upper and lower horizontal walls, while the thermal lines exhibit a similar pattern inside the fluid flow region adjacent to the obstacle. Such variations indicate that the conduction is dominant at low values of Ra. Meanwhile, as Ra increases, the isotherms spread more widely across the enclosure's center to its edges, and the thermal lines close to both cold and hot walls become denser. This suggests that convection is the primary mode of heat convection at larger Ra values. Therefore, as Ra increases, heat convection also increases. A dense thermal boundary layer also exists close to the cavity's hot walls; as Ra increases, this layer thins out, suggesting a faster rate of heat transference. These outcomes are highly consistent with the findings of Rehman *et al.* [12] and Nayak *et al.* [15]. Furthermore, for isolines of micro-rotation for distinct values of Ra, an identical observation to streamlines having less magnitude is noticed. Meanwhile, the adverse effect of buoyancy forces on S_{LEG} and Be_{local} is shown in Figure 3. The three factors that contribute to entropy generation are the magnetic field, the transfer of heat, and the friction of fluids. Figure 3 indicates that the production of entropy occurs only in the corner region of the heated walls of the enclosure, as well as at corners of the heated obstacle, particularly for low Ra values. The production of entropy is enhanced as Ra increases. Furthermore, Figure 3 illustrates that Be_{local} for distinct Ra

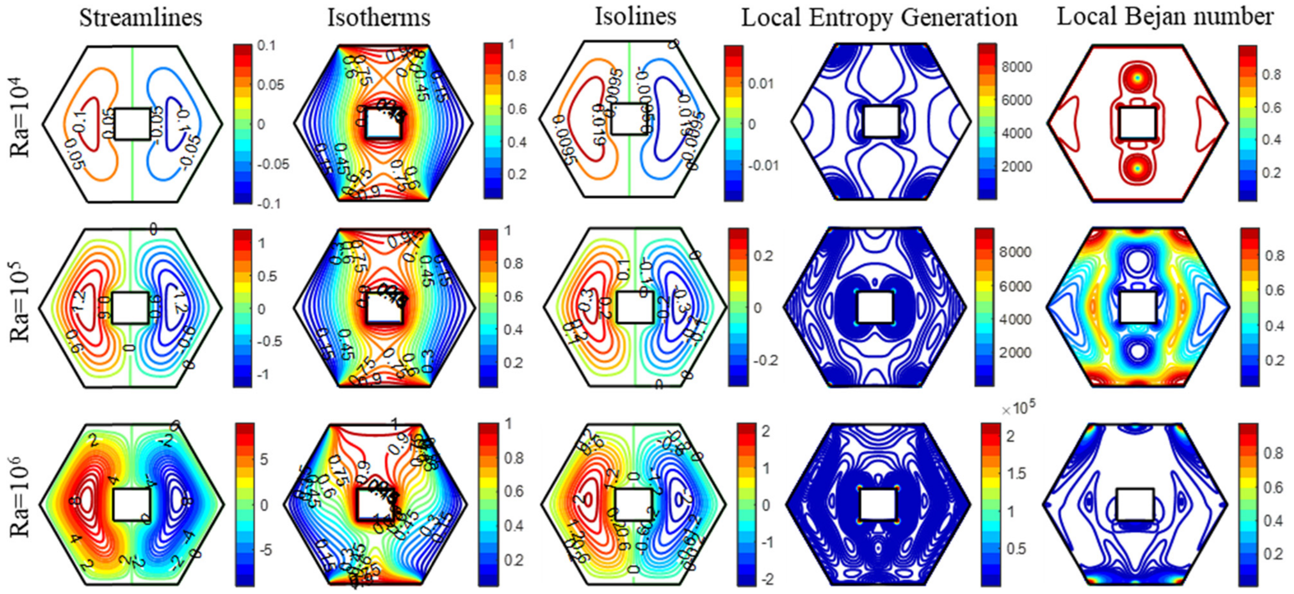

Figure 3: Influence of Ra on the flow, thermal, and local irreversibility profiles when Da = 10^{-3}, Ha = 10, K_0 = 2, and ϕ_{hnf} = 0.04.

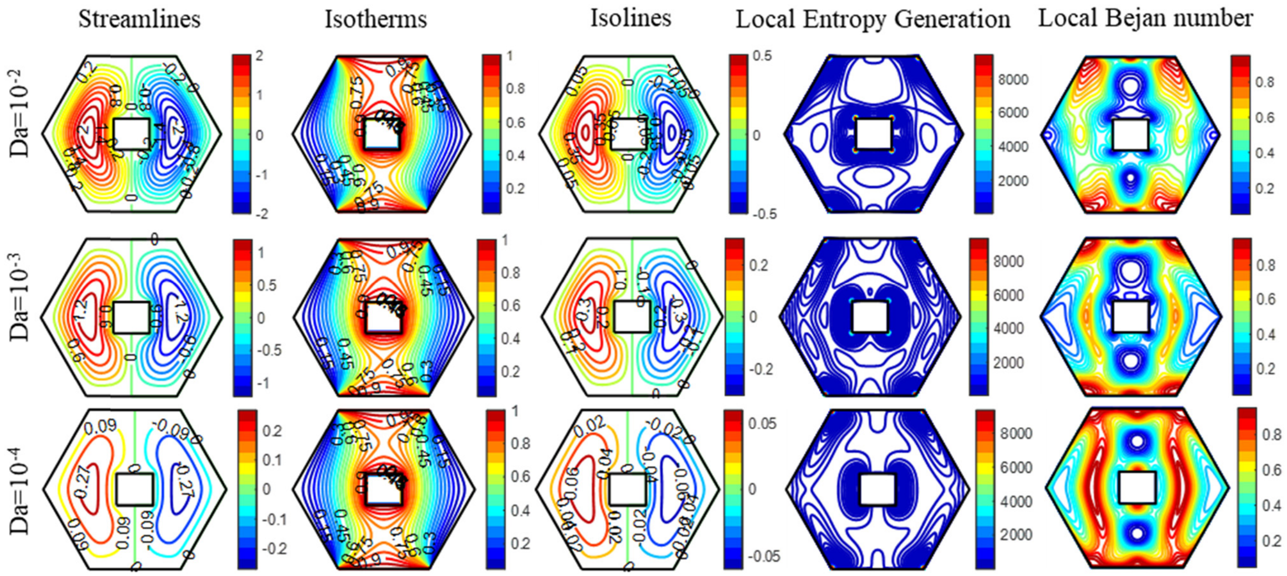

Figure 4: Influence of Da on the flow, thermal, and local irreversibility profiles when Ra = 10^5, K_0 = 2, Ha = 10, and ϕ_{hnf} = 0.04.

values. The $\mathrm{Be}_{\mathrm{local}}$ measures local heat transfer irreversibility by the total local irreversibility caused by the transfer of heat, fluid friction, and magnetic forces. The highest values of $\mathrm{Be}_{\mathrm{local}}$ are typically observed in an area characterized by extreme temperature variations with low-velocity magnitude and *vice versa*. At lower Ra, $\mathrm{Be}_{\mathrm{avg}}$ in the enclosure is approximately 1, indicating that thermal effect-related irreversibility is dominant. At exceptionally high Ra values, the rate of heat convection is increased, and velocity variations inside the system are enhanced. As a result, there is a reduction in $\mathrm{Be}_{\mathrm{avg}}$. Hence, thermal irreversibility is no longer the primary factor that contributes to total irreversibility. Figure 4 displays the influence of porous media on the streamlines, isotherms, isolines of micro-rotation, local entropy generation, and local Bejan number, precisely associated with the Darcy number (Da). A symmetrical arrangement of heated obstacles along the vertical centerline of the enclosure results in two circulation zones circulating clockwise and anticlockwise. A decline in Da leads to a decrease in permeability, resulting in a decrease in both the strength and size of the cell circulation and an increase in the barrier to the fluid flow. The magnitude of the streamlines reduces from $\psi_{\max}$ = 2 to 0.27 as the Da decreases from 10^{-2} to 10^{-4}, as depicted in Figure 4. The isotherms around a heated obstacle that relate to a smaller Da value are compact compared with the outcomes at higher Da values. It is prominent that reducing the Da lowers the porousness of the material, which in turn causes the fluid to keep more heat, creating a higher temperature zone close to the heated obstacle; as a result, the fluid's temperature increases, and heat convection drops significantly. Additionally, Figure 4 shows the reduction in the magnitude and size of isolines of micro-rotation as the permeability of the porous material decreases. Also, S_{LEG} becomes more intense near heated walls of the cavity and heated obstacle's corner, as shown in Figure 4. S_{LEG} attains its highest possible value near the corners of the hot obstacle and decreases as the Da value decreases. The permeability of the porous medium significantly affects the $\mathrm{Be}_{\mathrm{local}}$. It has been observed that reducing Da from 10^{-2} to 10^{-4} leads to an expansion of the zone wherein thermal irreversibility predominates.

The adverse effect of Hartmann number (Ha) on streamlines, isotherms, isolines of micro-rotation, local entropy generation, and local Bejan number is displayed in Figure 5. Figure 5 shows that the intensity of the flow's movement decreases as the Ha value increases. Additionally, the fluid velocities become much slower as Ha improves. The plausible explanation for this is that the exertion of a magnetic field produces a Lorentz force, which diminishes the movement of the fluid. Furthermore, the central cells experienced a noticeable impact on the magnetic field, while no significant alterations were observed in the cells located close to the boundary edges. Meanwhile, Figure 5 illustrates the effect of Ha on isotherms throughout the cavity. The results demonstrate that the isotherm contours exhibit symmetry around heated obstacles and indicate the presence of regions of high temperature near the heated walls. This is because Ha has a negligible impact on the existing thermal boundary layer. Furthermore, the isotherms exhibit nearly parallel orientation for higher Ha values and have an equal distribution within the enclosure; hence, a decreased convection process and a predominance of heat transfer through conduction are

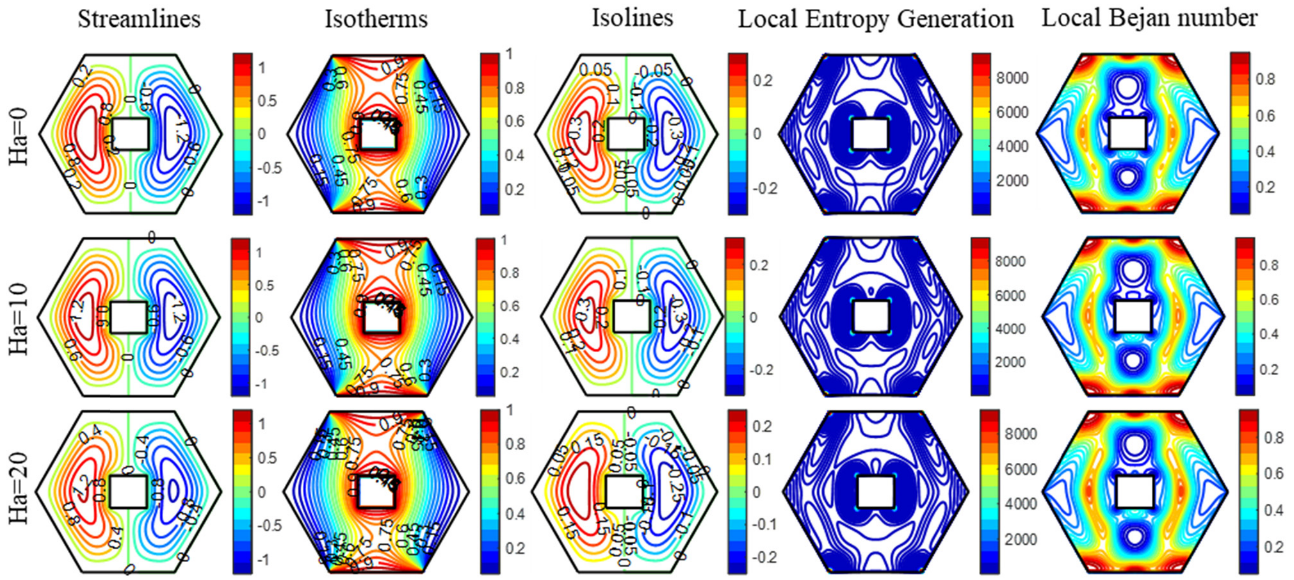

Figure 5: Influence of Ha on the flow, thermal, and local irreversibility profiles when Ra = 10^5, K_0 = 2, Da = 10^{-3}, and ϕ_{hnf} = 0.04.

observed. These occurrences are anticipated as the external magnetic field tends to diminish the convection process for heat transfer. Figure 5 demonstrates a decrease in the extent of isolines of micro-rotation as Ha advances. The increase in Ha restricts the movement of the fluid by minimizing the Lorentzian force that drives the flow. The Lorentzian force has a profound effect on the flow, which in turn affects the angular momentum. As a result, the strength of the "isolines of micro-rotation" decreases with Ha. At Ha = 0, the highest values of irreversibility resulting from heat transfer are observed near the heated walls of the enclosure and at corners of a heated obstacle, where the temperature gradient is highest in these locations, whereas frictional irreversibilities occur near the slanted wall of the cavity. The augmentation in Ha leads to a boost in Joule heating and subsequently enhances the irreversibility caused by the magnetic field. As a result, there is an equivalent increase in S_{Total} and a decrease in Be_{avg}, which is significant and is given in Table 4.

In the discipline of microfluidics, the granules' translation and spin lead to fluid movement. Feng *et al.* [40] discovered that the antisymmetric component of the deviatoric stress is responsible for the motion of the liquid at the suspension scale. Vortex viscosity κ introduces a dimensionless parameter known as the vortex viscosity parameter (K_0). Analysis of fluid rheology is carried out employing the material parameter K_0. K_0 = 0, for a Newtonian fluid. Figure 6 illustrates the effects of non-Newtonian rheology on streamlines, isotherms, isolines of micro rotation, S_{Total}, and Be_{local}. There is a significant decrease in streamline bunching as K_0 is increased. A reduction in $\psi_{\max}$ from 1.2 to 0.6 occurs when K_0 increases from 2 to 7.5. The results are correlated with the findings that as K_0 increases, the fluid's dynamic viscosity simultaneously improves as the velocity of the fluid decreases. As K_0 increases, the isotherm lines become straight. For a relatively low value of K_0, the isotherm lines close to the heated obstacle are dense compared with a high value of K_0.

Therefore, this leads to the enlargement of the high-temperature zone within the enclosure. The phenomenon indicates a decrease in heat transfer due to a boost in the resistance to fluid motion, arising from the improvement in dynamic viscosity through an increase in vortex viscosity. Additionally, Figure 6 illustrates a reduction in size and intensity of isolines of micro-rotation as K_0 increases. Moreover, the consequences of the fluid's rheology on the

Table 4: Impacts of numerous factors on the average Nusselt number and irreversibility analysis

Ra	Da	Ha	K_0	ϕ_{hnf}	Nu_{ABW}	S_{Total}	Be_{avg}
10^5	10^{-3}	10	2	0.04	10.700	44.5925	0.48581
10^4	—	—	—	—	9.9668	21.5877	0.99203
10^6	—	—	—	—	15.2542	1227.727	0.02362
10^5	10^{-2}	—	—	—	11.1008	44.5843	0.49405
—	10^{-4}	—	—	—	10.1031	30.2198	0.70900
—	10^{-3}	0	—	—	10.7232	45.6050	0.47539
—	—	20	—	—	10.6377	41.9858	0.51499
—	—	10	5	—	10.3874	38.9178	0.55278
—	—	—	7.5	—	10.2575	35.0344	0.61279
—	—	—	2	0.02	10.5334	44.9980	0.47253
—	—	—	—	0.00	10.3743	45.4001	0.45993

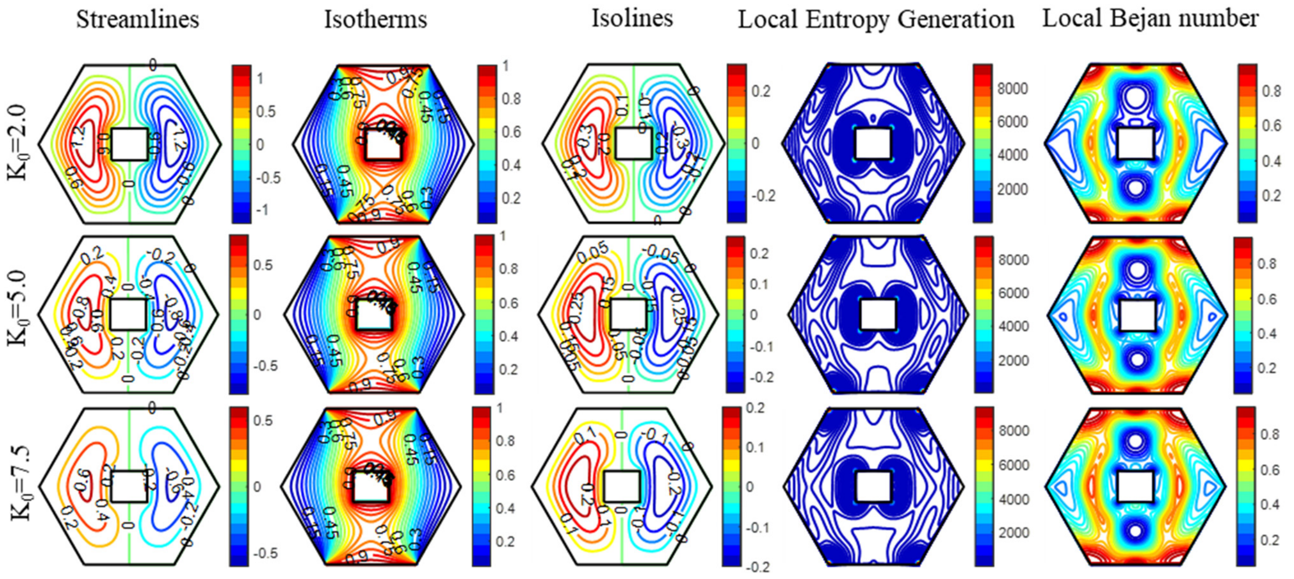

Figure 6: Influence of K_0 on the flow, thermal, and local irreversibility profiles when Ra = 10^5, Da = 10^{-3}, Ha = 10, and ϕ_{hnf} = 0.04.

generation of entropy by raising K_0 is demonstrated in Figure 6. The dominance of frictional irreversibilities is evident throughout the enclosure, except near the corners of heated walls and heated obstacles, where thermal irreversibilities prevail. An increase in K_0 leads to a substantial reduction in frictional irreversibilities. The analysis of $\mathrm{Be}_{\mathrm{local}}$ contours reveals that the influence of frictional irreversibility near the slanted vertical walls decreases as K_0 increases.

Figure 7 provides a detailed explanation of the consequences of nanoparticle volume concentration (ϕ_{hnf}) in the fluid. The appearance of the circulating cells near the middle of the circular eddy is significantly influenced by an increase in ϕ_{hnf}, while no significant alterations were observed close to the outermost cells. The streamline's denseness decreases as ϕ_{hnf} improves. This demonstrates the decrease in fluid movement resulting from the resistance in circulation triggered by the presence of nanoparticles. Comparatively, Figure 7 shows that ϕ_{hnf} has minimal effect on the shape of isotherm variation. Moreover, the addition of nanoparticles into regular fluid enhances the thermal conductivity of the regular fluid. In addition, isotherm curvature reduces as ϕ_{hnf} increases from 0 to 4%, and the

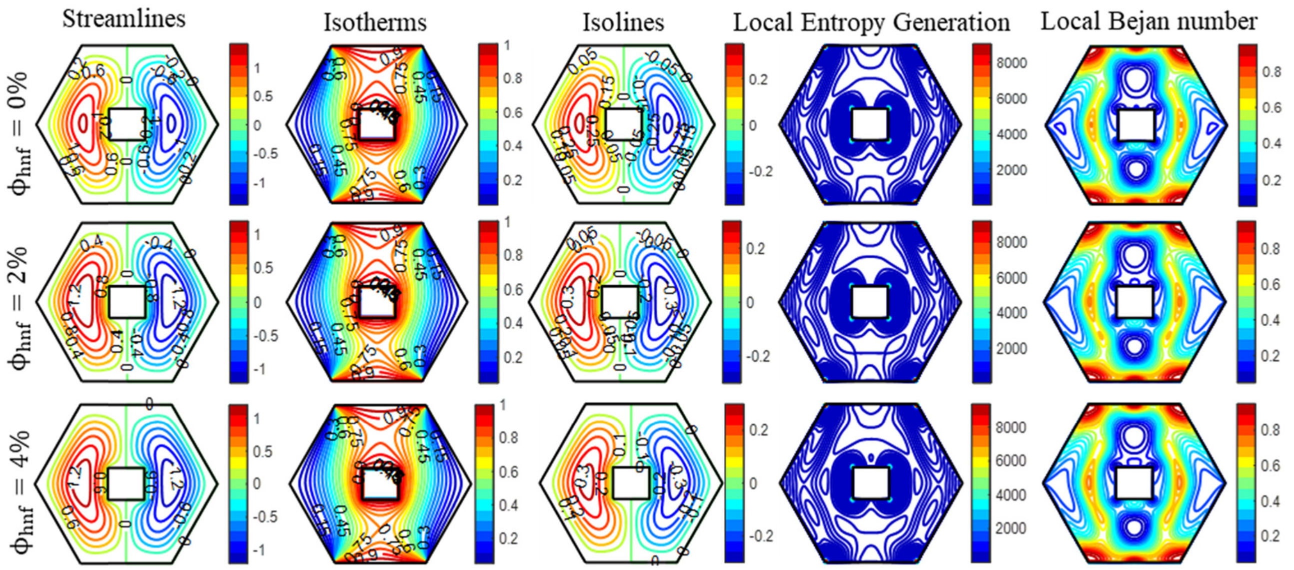

Figure 7: Influence of ϕ_{hnf} on the flow, thermal, and local irreversibility profiles when Ra = 10^5, Da = 10^{-3}, Ha = 10, and K_0 = 2.

thermal lines are concentrated close to the heated walls, suggesting that conductive heat transfer is the dominant mechanism. Additionally, it is noted that the isotherms exhibit a fairly symmetrical distribution throughout the enclosure. These results are consistent with the expected physical phenomena. It is also observed in Figure 7 that the effect of ϕ_{hnf} on the isolines is significant and increases the intensity of isolines with an increase in ϕ_{hnf}. The increase in the magnitude of ϕ_{hnf} reduces the rate of local entropy production within the cavity. A region near the inclined sidewalls and around the heated obstacle within the cavity shows that frictional forces dominate over thermal irreversibility. However, near the corners of heated walls, thermal irreversibilities are dominant. However, near heated walls and heated obstacles, thermal irreversibilities prevail. Furthermore, as ϕ_{hnf} increases the thermal irreversibility, which becomes more important than frictional irreversibility, as can be inferred from the Be_{local} contours.

Figure 8 demonstrates the influence of the placement of heated obstacles within the enclosure on the patterns of streamlines, isotherms, isolines of micro-rotation, S_{LEG} and Be_{local}. The values of the parameters chosen for this analysis are Ra = 10^5, Da = 10^{-3}, Ha = 10, K_0 = 2, and ϕ_{hnf} = 4%. It is observed that the existence of a thermally heated obstacle located either on the left or right side of the hexagonal cavity perturbs the symmetrical arrangement of streamlines and isolines of micro-rotation. The thermal irreversibilities become more prominent than the frictional irreversibilities in the vicinity of the slanted walls of the cavity when the heated obstacle approaches these walls.

By examining the data presented in Table 5, it is evident that when the thermally heated obstacle is positioned on either the left or right side of the enclosure, there is a slightly higher transmission of heat from the bottom wall and less entropy production throughout the enclosure, as compared to the case where the heated obstacle situated in the center of the hexagonal cavity. Whenever the thermally heated obstacle is near the bottom hot wall of the cavity, the heated zone surrounding the obstacle and

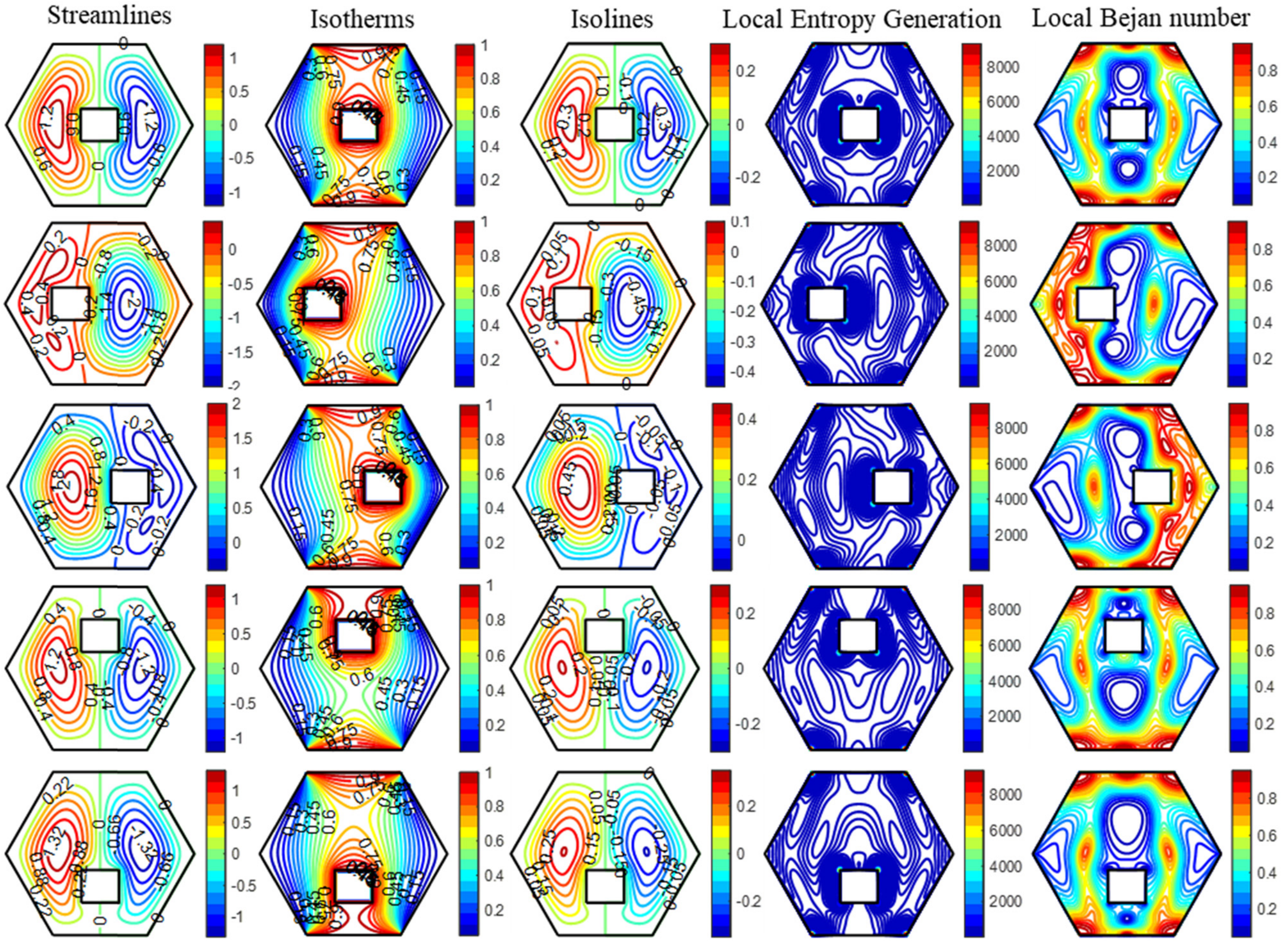

Figure 8: Influence of the position of heated obstacle on the flow, thermal, and local irreversibility profiles when Ra = 10^5, Da = 10^{-3}, Ha = 10, K_0 = 2, and ϕ_{hnf} = 4%.

Table 5: Effects of the location of thermally heated obstacle on the transference of heat and irreversibilities at Ra = 10^5, Ha = 10, K_0 = 2, Da = 10^{-3}, and ϕ_{hnf} = 4%

Location of heated obstacle	$\mathrm{Nu}_{\mathrm{ABW}}$	S_{Total}	$\mathrm{Be}_{\mathrm{avg}}$
Centrally aligned	10.7000	44.5925	0.48581
Left aligned	10.8105	44.3756	0.52380
Right aligned	10.8103	44.3804	0.52374
Top aligned	11.1495	38.2290	0.55040
Bottom aligned	9.43760	42.9494	0.49187

the region close to the bottom wall expands. Hence, a decline in the transference of heat is noticed from the bottom wall compared to all other configurations of the heated obstacle.

Furthermore, the data provided in Table 5 demonstrate significant enhancements in heat transfer and reduction in entropy generation when a thermally heated obstacle is positioned close to the upper wall, as opposed to alternative configurations of heated obstacles. This configuration signifies an optimal design for thermal devices, offering environmentally friendly and energy-efficient engineering solutions. Additionally, when a heated obstacle is close to the top wall, the region adjacent to the bottom wall and edges of the upper wall exhibits a $\mathrm{Be}_{\mathrm{avg}} \geq 0.5$. This indicates that thermal irreversibilities are more significant than frictional irreversibilities in this area. However, in the remaining cavity, frictional irreversibilities prevail over thermal irreversibilities. If there is a need to enhance the conveyance of heat through the cavity, the most effective configuration involves placing the heated obstacle in close proximity to the top wall. Table 4 displays the results for the impacts of numerous factors on average Nusselt number ($\mathrm{Nu}_{\mathrm{ABW}}$), total entropy generation (S_{Total}), and average Bejan number ($\mathrm{Be}_{\mathrm{avg}}$). The subsequent increase in Ha decreases $\mathrm{Nu}_{\mathrm{ABW}}$ and S_{Total} while increasing $\mathrm{Be}_{\mathrm{avg}}$. The boost in Ra from 10^4 to 10^6 and increases $\mathrm{Nu}_{\mathrm{ABW}}$ to a 53.05% extent. Meanwhile, $\mathrm{Nu}_{\mathrm{ABW}}$ experiences a reduction of 0.797% and 4.135% when Ha increases from 0 to 20 and K_0 from 2 to 7.5, respectively. Furthermore, nanoparticles enhance the "thermal conductivity" of the resulting HNF, so ϕ_{hnf} has a positive effect on $\mathrm{Nu}_{\mathrm{ABW}}$, resulting in a 3.14% increase in $\mathrm{Nu}_{\mathrm{ABW}}$ as ϕ_{hnf} increases from 0% to 4%. As mentioned earlier, a decrease in the porosity of the medium causes a reduction in the fluid's velocity. Furthermore, the data presented in Table 4 clearly demonstrate that this reduction in velocity allows the fluid to retain more heat, ultimately resulting in a fluid temperature and decrease in heat transfer.

Figure 9 illustrates the effect of Ra on the average Nusselt number ($\mathrm{Nu}_{\mathrm{ABW}}$), total entropy generation (S_{Total}),

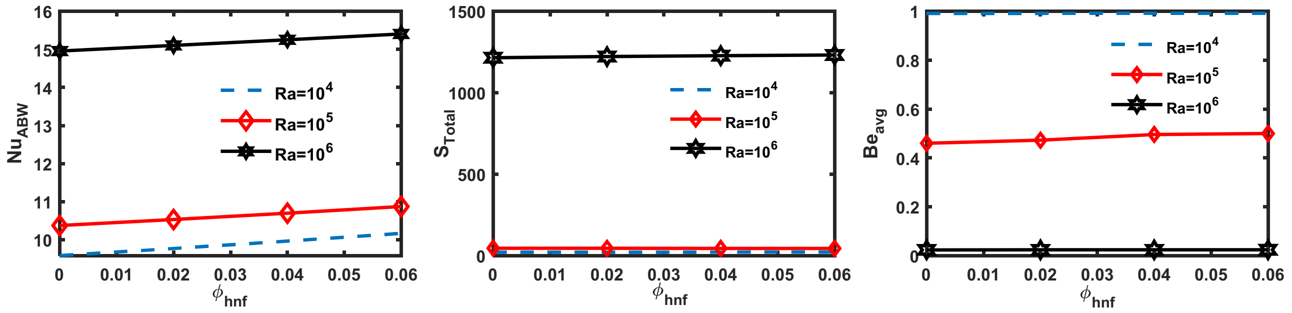

Figure 9: Variations in $\mathrm{Nu}_{\mathrm{ABW}}$, S_{Total}, and $\mathrm{Be}_{\mathrm{avg}}$ w.r.t. Ra and ϕ_{hnf} when Da = 10^{-3}, Ha = 10, and K_0 = 2.

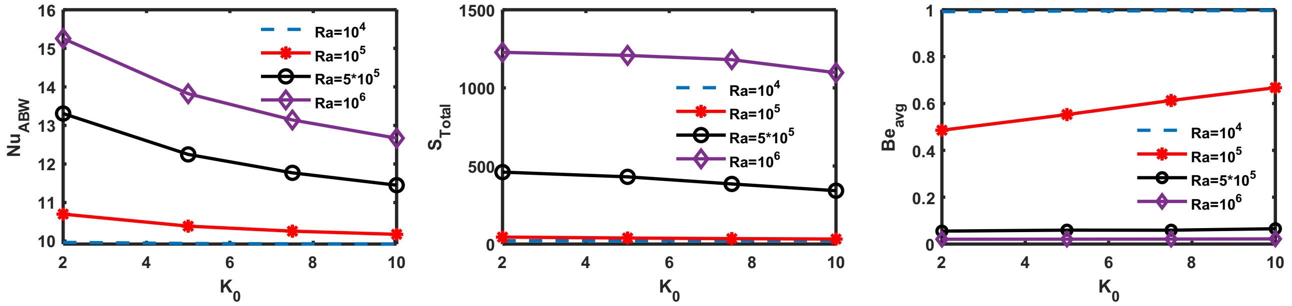

Figure 10: Variations in $\mathrm{Nu}_{\mathrm{ABW}}$, S_{Total}, and $\mathrm{Be}_{\mathrm{avg}}$ w.r.t. Ra and K_0 when Da = 10^{-3}, Ha = 10, and ϕ_{hnf} = 0.04.

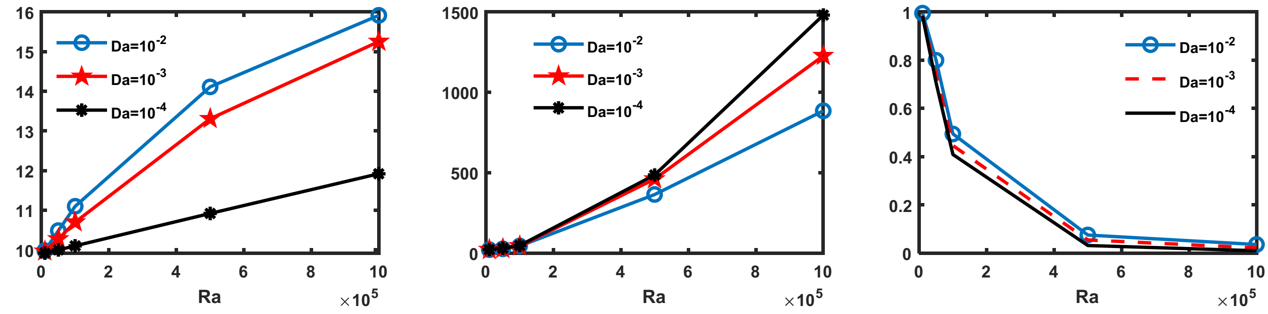

Figure 11: Variations in Nu_{ABW}, S_{Total}, and Be_{avg} w.r.t. Ra and Da when $K_0 = 2$, Ha = 10, and $\phi_{hnf} = 0.04$.

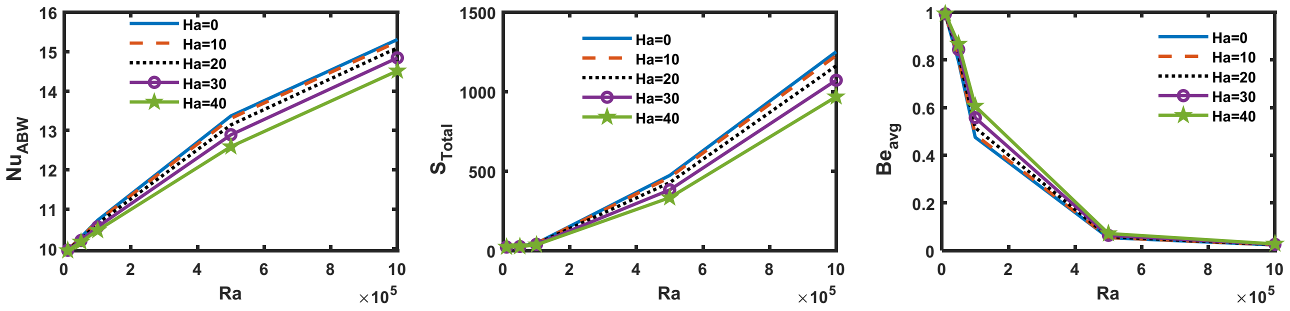

Figure 12: Variations in Nu_{ABW}, S_{Total}, and Be_{avg} w.r.t. Ra and Ha when $Da = 10^{-3}$, $K_0 = 2$, Ha = 10, and $\phi_{hnf} = 0.04$.

and average Bejan number (Be_{avg}) as ϕ_{hnf} increases. A significant improvement in buoyancy-assisted flow is brought about by the enhancement of Ra. This improvement has led to an increased rate of heat transfer through the bottom heated wall of the hexagonal cavity. Additionally, the increase of ϕ_{hnf} leads to an enhancement in the thermal conductivity of the base fluid, which in turn leads to an increase in heat convection. At small Ra values, such as Ra = 10^4, the average Bejan number is close to 1 for all ϕ_{hnf} values. This indicates that thermal irreversibilities are more significant than frictional irreversibilities, as viscous forces outweigh buoyancy forces. In addition, increasing the Ra value increased buoyancy forces, leading to frictional irreversibilities that surpass thermal. Figure 10 displays the corresponding changes in Nu_{ABW}, S_{Total}, and Be_{avg} with the variation in Ra and K_0. The results show that Nu_{ABW} and S_{Total} increase as Ra improves; however, a decrease is noticed in Nu_{ABW} and S_{Total} as K_0 increases due to an increase in $K_{0,}$ which additionally boosts the fluid's viscosity. Thermal irreversibilities improve as K_0 increases.

Figure 11 illustrates the impact of Ra and Da on Nu_{ABW}, S_{Total}, and Be_{avg}. It has been observed that a reduction in the value of Da leads to a reduction in Nu_{ABW}, although a boost in S_{Total} is observed. It is also depicted that both Nu_{ABW} and S_{Total} for associated Da is enhanced by an upsurge in Ra. Figures 12 and 13 demonstrate the significance of Lorentzian forces on the corresponding increase

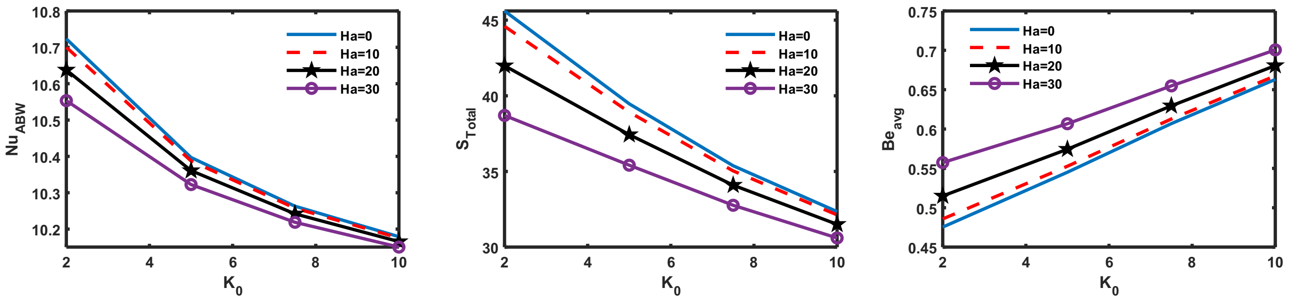

Figure 13: Variations in Nu_{ABW}, S_{Total}, and Be_{avg} w.r.t. K_0 and Ha when $Ra = 10^5$, $Da = 10^{-3}$, and $\phi_{hnf} = 0.04$.

of buoyancy forces and K_0, respectively. Furthermore, an increase in Ha decreases the initial prevalence of frictional irreversibilities over thermal irreversibilities. These results coincide substantially with the conclusions provided by Nayak *et al.* [15]. The outcomes clearly demonstrate that the generation of entropy and heat transmission can be significantly diminished by augmenting the values of Ha and K_0.

5 Conclusions

This work numerically examines the heat convection and entropy production in the presence of a heated obstacle within a porous hexagonal cavity subjected to a static magnetic field of strength B_0. Micropolar HNF, composed of TiO_2 and GO nanoparticles, was utilized to fill the cavity with water as the base fluid. The FDM associated with successive over-relaxation, successive relaxation, and Gauss–Seidel techniques are used to solve the dimensionless governing partial differential equations. The desired outcomes are computed using in-house developed MATLAB codes. The results were performed by employing a range of values: $10^4 \le \text{Ra} \le 10^6$, $0 \le \text{Ha} \le 20$, $0.00 \le \phi_{\text{hnf}} \le 0.04$, $2.0 \le K_0 \le 7.5$, and $10^{-2} \le \text{Da} \le 10^{-4}$. In light of the numerical outcomes and discussions, the main findings can be outlined as follows:

- An increase in Ra from 10^4 to 10^6 and ϕ_{hnf} from 0 to 4% leads to an enhancement in Nu_{ABW} to 53.05 and 3.14%, respectively. Meanwhile, Nu_{ABW} decreases approximately 0.797 and 4.135% as Ha increases from 0 to 20 and K_0 increases from 2 to 7.5, respectively.
- A decrease in porous medium's permeability (Da) from 10^{-2} to 10^{-4} leads to a decrease of 8.987 and 32.218% in Nu_{ABW} and S_{Total}.
- At low values, Ra, the entropy production is primarily associated with thermal irreversibilities. Conversely, at higher values of Ra, the maximum entropy originates owing to frictional irreversibilities.
- The increases in Ha and K_0 from 0 to 20 and 2 to 7.5 lead to a decrease of 7.935 and 21.434%, respectively, in S_{Total}.
- A substantial reduction of 1.779% in S_{Total} is observed as ϕ_{hnf} increases from 0 to 4%; however, there is a robust increase of 5587.16% as Ra increases from 10^4 to 10^6.
- As Ra increases, Be_{avg} diminishes consistently, whereas an increase in Ha, K_0, and ϕ_{hnf} improves Be_{avg}.
- As Ra and Da increase, there is an increased magnitude of S_{LEG}; despite this, S_{LEG} decreases at higher values of Ha and ϕ_{hnf}.
- A noteworthy enhancement in heat transfer and reduction in entropy generation is observed when a thermally heated obstacle is positioned close to the upper wall, as opposed to alternative configurations of heated obstacles. This configuration signifies an optimal design for thermal devices, offering environmentally friendly and energy-efficient engineering solutions.

The current study focuses on exploring the potential advantages of combining various nanoparticles, optimizing influential parameters, and improving designs to effectively regulate fluid flow, heat transfer, and production of entropy. The objective is to address the increasing need for improved thermal performance in the context of the new industrial age.

Future Scope: Future investigations may explore opportunities to enhance the study by considering different nanoparticles and the geometry of the heated obstacle. Additionally, exploring diverse thermal boundary conditions could further broaden the scope of inquiry.

Acknowledgments: The authors extend their appreciation to the Deanship of Research and Graduate Studies at King Khalid University for funding this work through a Large Research Project under grant number RGP2/122/45.

Funding information: This work was funded by the Deanship of Research and Graduate Studies at King Khalid University through a Large Research Project under grant number RGP2/122/45.

Author contributions: All authors have accepted responsibility for the entire content of this manuscript and approved its submission.

Conflict of interest: The authors state no conflict of interest.

Data availability statement: The datasets generated and/or analysed during the current study are available from the corresponding author on reasonable request.

References

[1] Choi SU, Eastman JA. Enhancing thermal conductivity of fluids with nanoparticles. Argonne, IL (United States): Argonne National Lab. (ANL); 1995.

[2] Mansour MA, Gorla RS, Siddiqa S, Rashad AM, Salah T. Unsteady MHD natural convection flow of a nanofluid inside an inclined square cavity containing a heated circular obstacle. Int J Nonlinear Sci Numer Simul. 2023;24(1):37–55.

[3] Saha T, Islam T, Yeasmin S, Parveen N. Thermal influence of heated fin on MHD natural convection flow of nanofluids inside a wavy square cavity. Int J Thermofluids. 2023;18:100338.

[4] Saleem KB, Marafie AH, Al-Farhany K, Hussam WK, Sheard GJ. Natural convection heat transfer in a nanofluid filled l-shaped enclosure with time-periodic temperature boundary and magnetic field. Alex Eng J. 2023;69:177–91.

[5] Weng L, Rahmani A, Sajadi SM, Kumar A, Ulloa N, Abdulameer SF, et al. Simulation of natural convection of nanofluid inside a square cavity using experimental data by lattice Boltzmann method. Ain Shams Eng J. 2024;15(5):102711.

[6] Wong KV, De Leon O. Applications of nanofluids: Current and future. Adv Mech Eng. 2010;2:519659.

[7] Jana S, Salehi-Khojin A, Zhong WH. Enhancement of fluid thermal conductivity by the addition of single and hybrid nano-additives. Thermochim Acta. 2007;462(1–2):45–55.

[8] Rashidi MM, Nazari MA, Mahariq I, Assad ME, Ali ME, Almuzaiqer R, et al. Thermophysical properties of hybrid nanofluids and the proposed models: An updated comprehensive study. Nanomaterials. 2021;11(11):3084.

[9] Acharya N. On the flow patterns and thermal control of radiative natural convective hybrid nanofluid flow inside a square enclosure having various shaped multiple heated obstacles. Eur Phys J Plus. 2021;136(8):889.

[10] Acharya N. Magnetically driven MWCNT-Fe_3O_4-water hybrid nanofluidic transport through a micro-wavy channel: A novel MEMS design for drug delivery application. Mater Today Commun. 2024;38:107844.

[11] Manna NK, Biswas N, Mandal DK, Yadav CK. Steady and unsteady dynamics of magneto-nanofluidic flow in a bottom-heated top-cooled recto-triangular thermal system. Heat Transf Eng. 2024;1–21. doi: 10.1080/01457632.2024.2317611.

[12] Rehman KU, Malik MY, Al-Mdallal QM, Al-Kouz W. Heat transfer analysis on buoyantly convective non-Newtonian stream in a hexagonal enclosure rooted with T-Shaped flipper: hybrid meshed analysis. Case Stud Therm Eng. 2020;21:100725.

[13] Khan Y, Majeed AH, Shahzad H, Awan FJ, Iqbal K, Ajmal M, et al. Numerical computations of non-newtonian fluid flow in hexagonal cavity with a square obstacle: a hybrid mesh–based study. Front Phys. 2022;10:891163.

[14] Faraz N, Nisar MS, Khan Y, Hussain A, Iqbal K. Natural convection of Cu-H_2O nanofluid inside hexagonal enclosure fitted with a square cavity with a non-uniformly heated wall (s). Results Phys. 2023;51:106648.

[15] Nayak MK, Dogonchi AS, Rahbari A. Free convection of Al_2O_3-water nanofluid inside a hexagonal-shaped enclosure with cold diamond-shaped obstacles and periodic magnetic field. Case Stud Therm Eng. 2023;50:103429.

[16] Bejan A. A study of entropy generation in fundamental convective heat transfer. J Heat Transf. 1979;101(4):718–25.

[17] Bejan A. Second-law analysis in heat transfer and thermal design. Adv Heat Transf. 1982;15:1–58.

[18] Baytaş AC. Entropy generation for natural convection in an inclined porous cavity. Int J Heat Mass Transf. 2000;43(12):2089–99.

[19] Acharya N. On the hydrothermal behavior and entropy analysis of buoyancy driven magnetohydrodynamic hybrid nanofluid flow within an octagonal enclosure fitted with fins: Application to thermal energy storage. J Energy Storage. 2022;53:105198.

[20] Ahlawat A, Sharma MK. Effects of heated block comprised porous stratum and micropolar hybrid nanofluid on convective heat transfer and entropy generation in a square enclosure. Heat Transf. 2022;51(6):5320–47.

[21] Ahlawat A, Sharma MK. MHD micropolar hybrid nanofluid flow through an annulus with discrete surface heaters: A study for optimal heat convection. Heat Transf. 2023;52(1):495–525.

[22] Manna NK, Saha A, Biswas N, Ghosh K. Effects of enclosure shape on MHD nanofluid flow and irreversibility in different shaped systems under fluid volume constraint. Int J Numer Methods Heat Fluid Flow. 2024;34(2):666–708.

[23] Eringen AC. Simple microfluids. Int J Eng Sci. 1964;2(2):205–17.

[24] Eringen AC. Theory of micropolar fluids. J Math Mech. 1966;1:1–18.

[25] Papautsky I, Brazzle J, Ameel T, Frazier AB. Laminar fluid behavior in microchannels using micropolar fluid theory. Sens Actuat A – Phys. 1999;73(1-2):101–8.

[26] Tayebi T, Dogonchi AS, Chamkha AJ, Hamida MB, El-Sapa S, Galal AM. Micropolar nanofluid thermal free convection and entropy generation through an inclined I-shaped enclosure with two hot cylinders. Case Stud Therm Eng. 2022;31:101813.

[27] Ahlawat A, Sharma MK, Rashidi MM, Sheremet MA. Entropy production minimization and heat transfer enhancement in a cavity filled with micropolar hybrid nanofluid under an influence of discrete heaters and uniform magnetic field. J Ther Anal Calorim. 2023;148(20):10803–20.

[28] Pal D, Mandal G. Hydromagnetic convective–radiative boundary layer flow of nanofluids induced by a non-linear vertical stretching/shrinking sheet with viscous–Ohmic dissipation. Powder Technol. 2015;279:61–74.

[29] Al-Sankoor K, Al-Gayyim H, Al-Musaedi S, Asadi Z, Ganji DD. Analytically investigating of heat transfer parameters with presence of graphene oxide nanoparticles in Williamson-magnetic fluid by AGM and HPM methods. Case Stud Therm Eng. 2021;27:101236.

[30] Mansour MA, Ahmed SE, Aly AM, Raizah ZA, Morsy Z. Triple convective flow of micropolar nanofluids in double lid-driven enclosures partially filled with LTNE porous layer under effects of an inclined magnetic field. Chin J Phys. 2020;68:387–405.

[31] Ahmadi G. Self-similar solution of incompressible micropolar boundary layer flow over a semi-infinite plate. Int J Eng Sci. 1976;14(7):639–46.

[32] Rees DA, Pop I. Free convection boundary-layer flow of a micropolar fluid from a vertical flat plate. IMA J Appl Math. 1998;61(2):179–97.

[33] Ishak A, Nazar R, Pop I. Boundary-layer flow of a micropolar fluid on a continuously moving or fixed permeable surface. Int J Heat Mass Transf. 2007;50(23–24):4743–8.

[34] Ghalambaz M, Doostani A, Izadpanahi E, Chamkha AJ. Conjugate natural convection flow of Ag–MgO/water hybrid nanofluid in a square cavity. J Ther Anal Calorim. 2020;139(3):2321–36.

[35] Maxwell JC. A treatise on electricity and magnetism. Oxford: Clarendon Press; 1873.

[36] Brinkman HC. The viscosity of concentrated suspensions and solutions. J Chem Phys. 1952;20(4):571–81.

[37] Seyyedi SM, Dogonchi AS, Hashemi-Tilehnoee M, Waqas M, Ganji DD. Entropy generation and economic analyses in a nanofluid filled L-shaped enclosure subjected to an oriented magnetic field. Appl Therm Eng. 2020;168:114789.

[38] Ali MM, Alim MA, Ahmed SS. Magnetohydrodynamic mixed convection flow in a hexagonal enclosure. Procedia Eng. 2017;194:479–86.

[39] Ilis GG, Mobedi M, Sunden B. Effect of aspect ratio on entropy generation in a rectangular cavity with differentially heated vertical walls. Int Commun Heat Mass Transf. 2008;35(6):696–703.

[40] Feng S, Graham AL, Abbott JR, Brenner H. Antisymmetric stresses in suspensions: Vortex viscosity and energy dissipation. J Fluid Mech. 2006;563:97–122.

Appendix-I

1. Stream function equation in a discretized form:

$$\psi(i,j) = \frac{1}{4}[h^2\psi(i,j) + \psi(i+1,j) + \psi(i-1,j) + \psi(i,j+1) + \psi(i,j-1)]$$

2. Vorticity equation in a discretized form:

$$\omega(i,j) = \frac{1}{A_1}[-C_{11} + A_2C_{12} - A_3C_{13} + A_4C_{14} + A_5C_{15}]$$

$$A_1 = \left[\frac{16\epsilon\mathrm{Pr}\rho_\mathrm{f}}{\rho_\mathrm{hnf}}\left\{\frac{1}{(1-\phi_\mathrm{hnf})^{2.5}} + K_0\right\} + \frac{4 \quad h^2\epsilon^2\mathrm{Pr}\rho_\mathrm{f}}{\rho_\mathrm{hnf} \quad (1-\phi_\mathrm{hnf})^{2.5}\mathrm{Da}}\right];$$

$$A_2 = \frac{4\epsilon\mathrm{Pr}\rho_\mathrm{f}}{\rho_\mathrm{hnf}}\left\{\frac{1}{(1-\phi_\mathrm{hnf})^{2.5}} + K_0\right\};$$

$$A_3 = \frac{4\mathrm{K}_0\epsilon^2\mathrm{Pr}\rho_\mathrm{f}}{\rho_\mathrm{hnf}}; \quad A_4 = \frac{2\mathrm{h}\varepsilon^2\mathrm{PrRa}(\rho\beta)_\mathrm{hnf}}{\rho_\mathrm{hnf}\beta_\mathrm{f}};$$

$$A_5 = 4\left(\frac{\sigma_\mathrm{hnf}}{\sigma_\mathrm{f}}\right)\left(\frac{\rho_\mathrm{f}}{\rho_\mathrm{hnf}}\right)\mathrm{Ha}^2\mathrm{Pr}\varepsilon^2$$

$$C_{11} = (\psi(i,j+1) - \psi(i,j-1))(\omega(i+1,j) - \omega(i-1,j)) - (\psi(i+1,j) - \psi(i-1,j))(\omega(i,j+1) - \omega(i,j-1))$$

$$C_{12} = (\omega(i+1,j) + \omega(i-1,j) + \omega(i,j+1) + \omega(i,j-1))$$

$$C_{13} = (N(i+1,j) + N(i-1,j) + N(i,j+1) + N(i,j-1) - 4N(i,j))$$

$$C_{14} = (\theta(i+1,j) - \theta(i-1,j))$$

$$C_{15} = \psi(i+1,j) - 2\psi(i,j) + \psi(i-1,j)$$

3. Angular momentum equation in a dimensionless form:

$$N(i,j) = \frac{1}{(4A_9 + A_{10})}[-D_{11} + A_9D_{12} + A_{11}\omega(i,j)]$$

$$A_9 = \frac{4\epsilon\mathrm{Pr}\rho_\mathrm{f}}{\rho_\mathrm{hnf}}\left\{\frac{1}{(1-\phi_\mathrm{hnf})^{2.5}} + \frac{K_0}{2}\right\};$$

$$\mathrm{A}_{10} = \frac{8\mathrm{Pr}h^2 \quad K_0 \quad \varepsilon\,\chi\rho_\mathrm{f}}{\rho_\mathrm{hnf}}; \quad \mathrm{A}_{11} = \frac{4\mathrm{Pr}\rho_\mathrm{f}K_0\chi}{\rho_\mathrm{hnf}}$$

$$D_{11} = (\psi(i,j+1) - \psi(i,j-1))(N(i+1,j) - N(i-1,j)) - (\psi(i+1,j) - \psi(i-1,j))(N(i,j+1) - N(i,j-1)).$$

$$D_{12} = (N(i+1,j) + N(i-1,j) + N(i,j+1) + N(i,j-1))$$

4. Energy equation in a discretized form:

$$\theta(i,j) = \left(\frac{1}{16}\right)\left(\frac{\alpha_\mathrm{f}}{\alpha_\mathrm{eff}}\right)\left[-T_{11} + \frac{4\alpha_\mathrm{eff}}{\alpha_\mathrm{f}}T_{12}\right]$$

$$T_{11} = (\psi(i,j+1) - \psi(i,j-1))(\theta(i+1,j) - \theta(i-1,j)) - (\psi(i+1,j) - \psi(i-1,j))(\theta(i,j+1) - \theta(i,j-1))$$

$$T_{12} = (\theta(i+1,j) + \theta(i-1,j) + \theta(i,j+1) + \theta(i,j-1)).$$

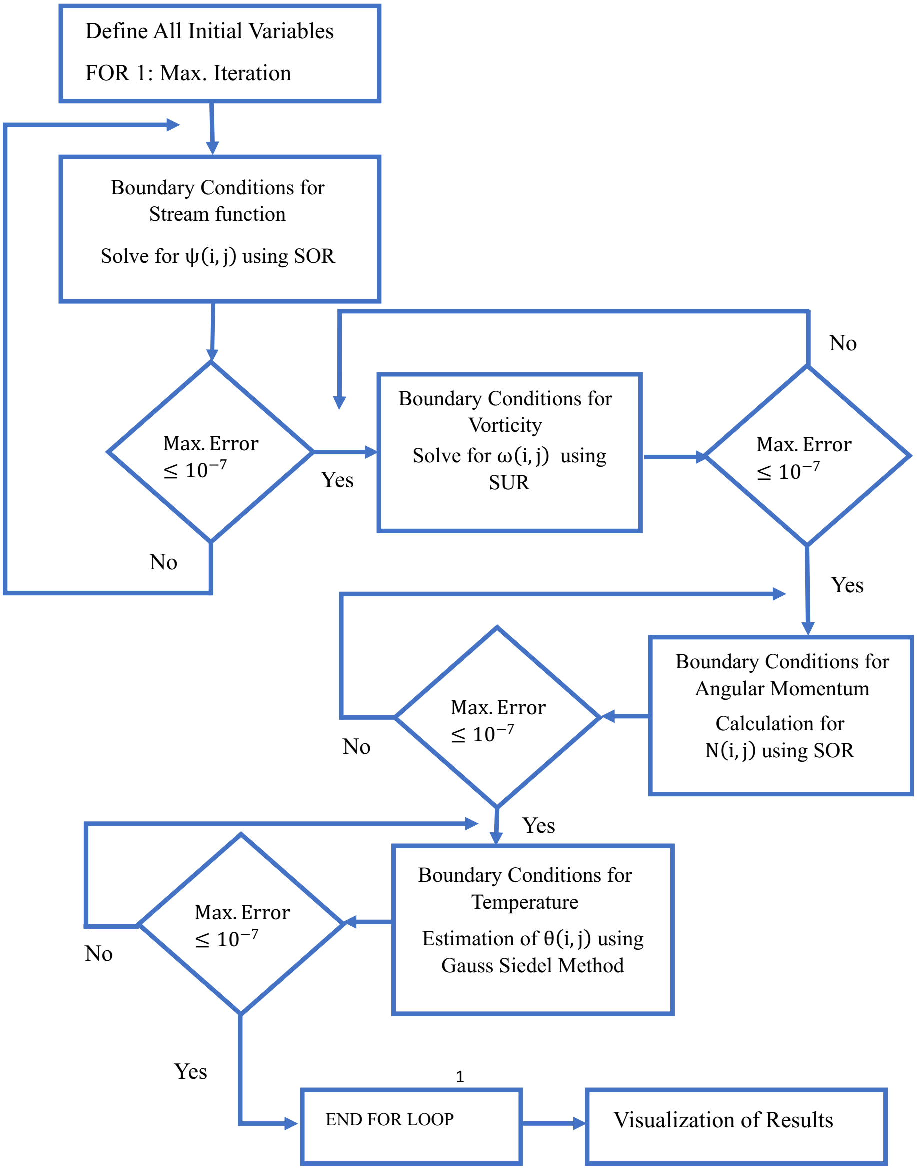
Define All Initial Variables
FOR 1: Max. Iteration
Boundary Conditions for Stream function
Solve for ψ(i, j) using SOR
Max. Error ≤ 10^{-7}
No
Yes
Boundary Conditions for Vorticity
Solve for ω(i, j) using SUR
Max. Error ≤ 10^{-7}
No
Yes
Boundary Conditions for Angular Momentum
Calculation for N(i, j) using SOR
Max. Error ≤ 10^{-7}
No
Yes
Boundary Conditions for Temperature
Estimation of θ(i, j) using Gauss Siedel Method
Max. Error ≤ 10^{-7}
No
Yes
1
END FOR LOOP
Visualization of Results